Modelling of ageing and atherosclerosis in arteries using ApoE$^{-/-}$ mice aortas

Tobias Waffenschmidt [a], Myriam Cilla [b], Pablo Sáez [c,d], Marta M. Pérez [e], Andreas Menzel [a], E. Peña [a,b,*],

[a] *Institute of Mechanics, Department of Mechanical Engineering, TU Dortmund. Germany*

[b] *Julius Wolff Institut. Charité - Universitätsmedizin Berlin. Germany*

[c] *Applied Mechanics and Bioengineering. I3A. University of Zaragoza. Spain.*

[d] *CIBER de Bioingeniería, Biomateriales y Nanomedicina (CIBER-BBN).*

[e] *Department of Anatomy, Embryology and Genetics, Veterinary Faculty. University of Zaragoza.*

Abstract

The objective of this work consists in the qualitative and quantitative analysis of ageing processes and associated plaque formation in mice arteries which are typical for atherosclerosis. Specifically, reliable information on the characteristic evolution of *pressure-stretch curves* due to the ageing effects are extracted from appropriate experiments. Furthermore, characteristic *age-dependent material parameters* are identified on the basis of a continuum-mechanics-based parameter optimization technique.

A computational continuum-mechanics-based framework is used to identify age-dependent material parameters on the basis of the experimental data. The basic deformation modes considered are represented by combined inflation and axial extension. We make use of an orthotropic constitutive model with two families of fibres and solve the underlying equilibrium conditions iteratively. We compute an objective function, represented by the difference between simulated and experimental data, which is minimized with respect to the material parameters.

The results indicate that the aorta-stiffness of the healthy control mice remains constant irrespective of the diet-time and age, respectively. In contrast, we observe significant deviations of the material parameters between the ApoE$^{-/-}$ and the control mice as well as for the different locations over the aorta which clearly underlines our observations from the experiments. With regard to the temporal evolution of the material parameters, we observe that the material parameters for the ApoE$^{-/-}$ mice aortas exhibit a characteristic, partially saturation-type, increase with respect to age.

Key words: grgrr

* Corresponding author. Estefanía Peña. Mechanical Engineering Department. c/ Maria de Luna s/n 50018. Zaragoza. Spain. Tel.: +34 876555233; Fax: +34 976762578

Email address: fany@unizar.es (E. Peña).

1 Introduction

Recent experimental studies show that atherosclerosis significantly modifies the mechanical properties of the arterial tissue. In this regard, a combination of inflammatory, biological and mechanical processes tend to remodel the arterial wall structure and composition, see, for instance, [30]. Although histopathological analyses of postmortem specimens provide important data on the histological features of ruptured human plaques ([2, 18]) more sophisticated representative animal studies of plaque rupture are required. Manifold animal species are commonly used to study the pathogenesis and potential treatment of the lesions of atherosclerosis, see [5, 11, 25, 26, 31] amongst others. However, since their introduction in the early 1990s, apolipoprotein E-deficient transgenic mice ($\text{ApoE}^{-/-}$ mice)—created by homologous recombination in embryonic stem cells—represent the most common animal species studied in connection with atherosclerosis, cf. [8, 21, 34]. This is essentially due to their rapid development of atherosclerotic lesions with histopathological progression, similar to those of humans, as reported by Plump et al. [24].

Studying the morphological changes and mechanical properties during atheroma plaque development is particularly important in order to understand the mechanisms of vascular adaptation in response to changes in physical stress. Several studies investigate the morphological, structural, and biochemical changes of the aorta as well as the relation between these changes and the mechanics of the aorta, see [9, 16, 20, 32, 33]. These studies confirm that the aorta increases its stenosis ratio, wall thickness, and mechanical stiffness during atherosclerosis. Most of these studies, however, mainly focus on the proximal aorta, and none of them systematically characterize the geometrical and mechanical properties along the entire length of the aorta. Even though Guo and Kassab [14] study the whole aorta, they exclusively focus on the common laboratory mice (C57BL/6J mice), irrespective of the fact that $\text{ApoE}^{-/-}$ mice represent the only genetically engineered species that develops extensive atherosclerotic lesions on a normal chow diet, cf. [17].

The modelling, simulation and experimental study of arteries and associated vascular diseases such as atherosclerosis is an area of current multidisciplinary research. In order to enable an individual patient-specific adaptation/modification of the medical treatment, it is necessary to understand the underlying mechanisms of atherosclerotic plaque evolution. In this context, the modelling and simulation becomes increasingly important. For the description of the purely mechanical and passive behavior of arteries, several numerical material models have already been developed in the past decades. However, the temporal evolution and evolution in these vessels, commonly referred to as *ageing*, has almost not discussed in the literature yet. Nevertheless, the incorporation of such ageing effects—in combination with the detection, description, and especially interaction with plaques—is of central importance for the understanding of atherosclerosis.

As patient-specific "experimental studies" are usually not feasible for human arteries, the *modelling and simulation of ageing phenomena* becomes increasingly important in order to improve the reliability of medical prognoses. We therefore consider continuum mechanics-based mate-

rial modelling and simulation approaches on the basis of the aforementioned experimental investigations, in order to validate and calibrate the models. To be specific, a computational continuum-mechanics-based framework is used to identify age-dependent material parameters on the basis of the experimental data. We consider an inhomogeneous boundary value problem allowing for large deformations, i.e. an incompressible thick-walled cylindrical tube, which is assumed to approximate a real artery. The basic deformation modes considered are represented by combined inflation and axial extension. We make use of an orthotropic constitutive model with two families of fibres and solve the underlying equilibrium conditions iteratively. We compute an objective function, represented by the difference between simulated and experimental data, which is minimized with respect to the material parameters. As a main objective, we aim at determining the characteristic age-dependent evolution of material parameters in time.

The scientistic objective of this work consists in the quantitative analysis of ageing processes and associated plaque formation in mouse arteries. These effects are typical for atherosclerosis. Specifically, reliable information on the evolution of *pressure-stretch curves* and *axial residual stretches* due to the ageing effects are extracted from extensive previous experimental investigations [7]. Furthermore, characteristic *age-dependent material parameters* are identified on the basis of a continuum-mechanics-based parameter optimization technique.

2 Materials and methods

2.1 Mechanical properties

Female apolipoprotein E-deficient transgenic mice ($\text{ApoE}^{-/-}$ mice) and common laboratory control mice (C57BL/6 mice) were previously used to measure the pressure-diameter relationship. We analyzed the progressive evolution of atherosclerotic lesions at three different locations of the aorta of (i) $\text{ApoE}^{-/-}$ mice put on a hyper-lipidic Western diet and (ii) C57BL/6 control mice put on a normal chow diet. Different sets of five $\text{ApoE}^{-/-}$ and control mice were sacrificed after 10, 20, 30 and 40 weeks of their associated diet. Inflation tests and axial residual stretch measurements were performed. The aorta, beginning at the aortic valve and ending at the common iliac bifurcation, was connected to a pump system via the ascending aorta, the mouse being cannulated with an 18-gauge needle at the beginning of the intercostal aorta. The pressure transducer was connected to the pressure circuit between the pump and the specimen at one end, and to the computer at the other. Information of the deformation of the aortic outer diameter, d_o, was provided by two high resolution cameras.

The aorta was preconditioned within three cycles from $0\,[mmHg] - 200\,[mmHg]$. Then, the perfusion pressure p_i is increased in steps of $25\,[mmHg]$ from $p_i = 0\,[mmHg] - 250\,[mmHg]$, cf. Guao et al. [14], while the outer diameter d_o along the trunk of the aorta at each pressure step is recorded. The vessel is subdivided into a series of short segments of approximately $3\,[mm] - 4\,[mm]$ length per segment, and the pressure-outer-diameter-relation for each of the segments is measured. From these relations, typical pressure-stretch-curves are determined by

evaluating the outer circumferential stretch λ_{θ_o} as the ratio of the current and referential outer diameters d_o and D_o, i.e.

$$\lambda_{\theta_o} = \frac{d_o}{D_o} \,. \tag{1}$$

The atheroma plaque development is not uniform along the vessel. Therefore, three different zones of the aorta are studied separately, i.e. the upper thoracic aorta, the lower thoracic aorta and the iliac/abdominal aorta. In order to measure the axial residual stretch λ_z, separated markers are fixed to the aorta. Axial lengths before and after harvesting are determined by measuring the distance between markers, obtaining the *in situ* and *ex situ* dimensions, respectively. Then, the residual axial stretch λ_z, defined as the ratio between the *in situ* and *ex situ* measured lengths, $\lambda_z = l_{\text{in-situ}}/l_{\text{ex-situ}} := l/L$, is computed, cf. García et al. [12]. Axial residual stretches are calculated for the whole aorta vessel. The morphological measurements are made using the ImageJ® software.

2.2 Computational framework

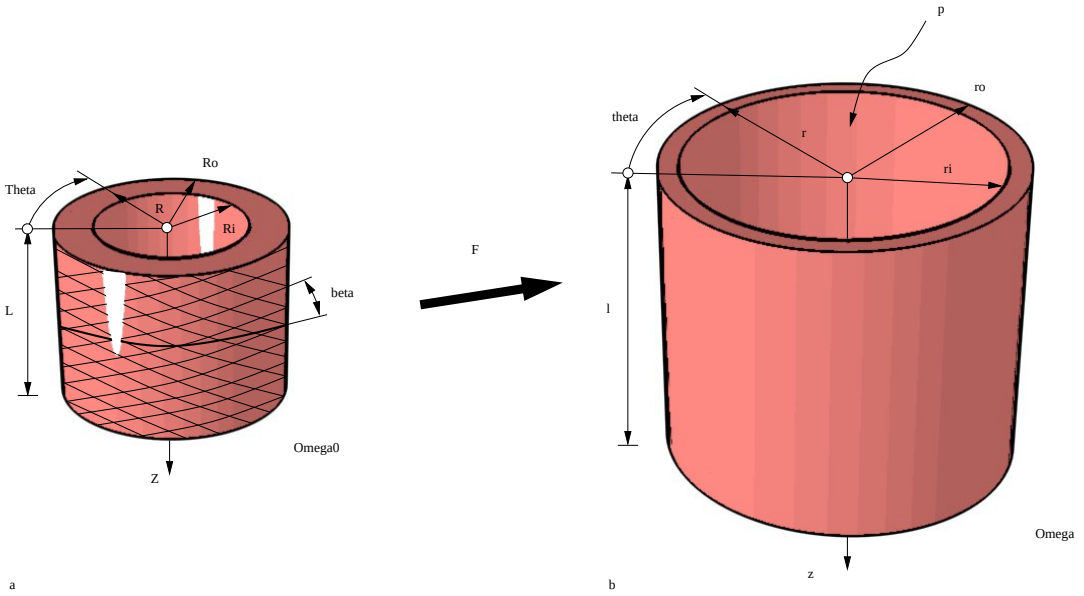

Fig. 1. Deformation modes of a thick-walled cylindrical tube: inflation (internal pressure p_i) and axial extension (axial stretch $\lambda_z = l/L$); arterial wall reinforced by two families of fibres with fibre angle β defined in (a) a stress-free reference configuration $\mathcal{B}_0$; (b) residually stressed and loaded current configuration $\mathcal{B}_t$.

This section deals with the computational continuum-mechanics-based framework used to identify age-dependent material parameters on the basis of the data obtained by the experimental framework described above in Section 2.1. Section 2.2.1 first discusses the basic kinematics of an incompressible thick-walled cylindrical tube, which is assumed to approximate a real artery. The basic modes of deformation considered are combined inflation and extension, see Ogden [22], Holzapfel et al. [15]. In Section 2.2.2, the underlying constitutive model adopted for the following investigations is briefly reviewed. To be specific, use of an orthotropic model with

two families of fibres is made as introduced by Holzapfel et al. [15]; for a general review on the modelling of fibre reinforced materials the reader is also referred to Spencer [28] and the contributions in Spencer [29] and Boehler [4]. Section 2.2.3 summarises the underlying equilibrium conditions. Finally, Section 2.2.4 deals with theoretical and algorithmic details with regard to the identification of the material parameters.

2.2.1 Basic kinematics

Position vectors of particles in an undeformed reference configuration $\mathcal{B}_0$ are denoted by $\boldsymbol{X}$ and position vectors in the deformed current configuration $\mathcal{B}_t$ at time t by $\boldsymbol{x} = \boldsymbol{\varphi}(\boldsymbol{X}, t)$. The kinematics of a thick-walled tube can conveniently be described by cylindrical polar coordinates. These coordinates are introduced as R, Θ and Z with respect to a chosen reference configuration $\mathcal{B}_0$ as well as r, θ and z with respect to the current configuration $\mathcal{B}_t$. An orthonormal referential and spatial frame, respectively, can be defined in terms of these coordinates as

$$\begin{aligned} \boldsymbol{E}_R(\Theta) &= \cos(\Theta)\,\boldsymbol{e}_1 + \sin(\Theta)\,\boldsymbol{e}_2\,, & \boldsymbol{e}_r(\theta) &= \cos(\theta)\,\boldsymbol{e}_1 + \sin(\theta)\,\boldsymbol{e}_2\,, & (2)\\ \boldsymbol{E}_\Theta(\Theta) &= -\sin(\Theta)\,\boldsymbol{e}_1 + \cos(\Theta)\,\boldsymbol{e}_2\,, & \boldsymbol{e}_\theta(\theta) &= -\sin(\theta)\,\boldsymbol{e}_1 + \cos(\theta)\,\boldsymbol{e}_2\,, & (3)\\ \boldsymbol{E}_Z &= \boldsymbol{e}_3\,, & \boldsymbol{e}_z &= \boldsymbol{e}_3\,. & (4) \end{aligned}$$

wherein $\{\boldsymbol{e}_1, \boldsymbol{e}_2, \boldsymbol{e}_3\}$ is a Cartesian frame fixed in space. The geometry of the tube considered is visualised in Figure 1 and its material and spatial settings are specified by

$$\begin{aligned} R_i \le R \le R_o\,, & \qquad r_i \le r \le r_o\,, & (5)\\ 0 \le \Theta \le 2\,\pi\,, & \qquad 0 \le \theta \le 2\,\pi\,, & (6)\\ 0 \le Z \le L\,, & \qquad 0 \le z \le l\,. & (7) \end{aligned}$$

where R_i, R_o and L represent the inner and outer radii and the length of the tube in a (undeformed) reference configuration $\mathcal{B}_0$ while r_i, r_o and l represent the corresponding quantities in the (deformed) current configuration $\mathcal{B}_t$; see Figure 1. With these quantities in hand, the deformation modes of inflation and extension of an incompressible tube can be represented by the spatial position vector

$$\boldsymbol{x} = \boldsymbol{\varphi}(\boldsymbol{X}, t) = r\,\boldsymbol{e}_r(\theta) + z\,\boldsymbol{e}_z \tag{8}$$

specified by means of

$$r = \sqrt{\frac{R^2 - R_i^2}{\lambda_z} + r_i^2}\,, \qquad \theta = \Theta\,, \qquad z = \lambda_z\,Z\,. \tag{9}$$

The parameter λ_z represents the axial (residual) stretch. Equation $(9)_1$ reflects the assumption of incompressibility: for the isochoric deformation of the tube considered the referential sub-volume $V(R) = \pi\,L\,[\,R^2 - R_i^2\,]$ coincides with the current sub-volume $v(r) = \pi\,l\,[\,r^2 - r_i^2\,]$ from which, together with $(9)_3$, equation $(9)_1$ can be concluded.

Representative deformation measures can be introduced with respect to the coordinates R, Θ, Z and r, θ, z. In particular, equation (8) is used together with $\nabla_{\boldsymbol{X}}\,[\bullet] = \partial_R\,[\bullet] \otimes \boldsymbol{E}_R +$

$R^{-1}\,\partial_\Theta[\bullet]\otimes\boldsymbol{E}_\Theta+\partial_Z[\bullet]\otimes\boldsymbol{E}_Z$ to introduce the deformation gradient $\boldsymbol{F}=\nabla_{\boldsymbol{X}}\boldsymbol{\varphi}$. For the present scenario, the deformation gradient reduces to

$$\boldsymbol{F}=\lambda_r\,\boldsymbol{e}_r\otimes\boldsymbol{E}_R+\lambda_\theta\,\boldsymbol{e}_\theta\otimes\boldsymbol{E}_\Theta+\lambda_z\,\boldsymbol{e}_z\otimes\boldsymbol{E}_Z\,, \tag{10}$$

where the radial and circumferential stretch are introduced as

$$\lambda_r=\frac{R}{r\,\lambda_z}\qquad\text{and}\qquad\lambda_\theta=[\lambda_r\lambda_z]^{-1}=\frac{r}{R}\,. \tag{11}$$

It is obvious that the matrix of coefficients of $\boldsymbol{F}$ becomes symmetric for the present deformation so that λ_r, λ_θ and λ_z take the interpretation as principal stretches in radial, circumferential and axial direction.

2.2.2 Constitutive model

In the following, the underlying constitutive model adopted for the following investigations is briefly reviewed. We apply an orthotropic model with two families of fibres as introduced by Holzapfel et al. [15]. The strain energy density of this model is assumed to additively decompose into an isotropic part Ψ_{iso}, representing the contribution of the non-collagenous ground material, and an anisotropic part Ψ_{ani}, representing the contributions of the different families of collagen fibres, i.e.

$$\Psi\Big(\boldsymbol{F},\boldsymbol{a}_{0\,i}\Big)=\Psi_{\text{iso}}\Big(\boldsymbol{F}\Big)+\Psi_{\text{ani}}\Big(\boldsymbol{F},\boldsymbol{a}_{0\,i}\Big)\,. \tag{12}$$

Moreover, $\boldsymbol{a}_{0\,i}$ denotes a set of $i=1,\dots,N$ referential unit-vectors characterising the fibre families. The isotropic part of the strain energy is specified by a common neo-Hookean format

$$\Psi_{\text{iso}}(\boldsymbol{F}\Big)=\frac{c}{2}\,[\,I_1-3\,]\,, \tag{13}$$

with

$$I_1=\boldsymbol{F}:\boldsymbol{F}=\lambda_\theta^2+\lambda_z^2+\lambda_\theta^{-2}\,\lambda_z^{-2} \tag{14}$$

for $J\doteq 1$. The anisotropic part adopted takes the following exponential form

$$\Psi_{\text{ani}}\Big(\boldsymbol{F},\boldsymbol{a}_{0\,i}\Big)=\frac{k_1}{2\,k_2}\sum_{i=1}^{N}\Big[\exp\Big(k_2\,\langle E_i\rangle^2\Big)-1\Big]\,, \tag{15}$$

wherein it is assumed that the fibres are mechanically equivalent. The notation $\langle\bullet\rangle=[\,|\bullet|+\bullet\,]/2$ reflects the Macaulay brackets. These allow activation of the fibre contributions in the tension regime only. To be specific, the referential strain measure E_i is introduced as

$$E_i=\boldsymbol{a}_i\cdot\boldsymbol{F}^{\text{t}}\cdot\boldsymbol{F}\cdot\boldsymbol{a}_i-1=I_{4\,i}-1\,. \tag{16}$$

Even though equation (16) does not include any dispersion of fibre contributions, the formulation can be extended to account for these as discussed in, for instance, Gasser et al. [13] and

Alastrue et al. [1]. The number of mechanically equivalent fibre families is restricted to $N = 2$ and, moreover, their initial orientations are assumed as

$$\boldsymbol{a}_{0\,1,2} = \sin\Big(\beta\Big)\,\boldsymbol{E}_Z \pm \cos\Big(\beta\Big)\,\boldsymbol{E}_\Theta\,, \tag{17}$$

Furthermore, one observes $E_1 = E_2 \doteq E$ and the invariant introduced in equation (16) can be expressed as

$$I_{4\,i} = \boldsymbol{a}_i \cdot \boldsymbol{F}^{\mathrm{t}} \cdot \boldsymbol{F} \cdot \boldsymbol{a}_i = \sin^2\Big(\beta\Big)\,\lambda_z^2 + \cos^2\Big(\beta\Big)\,\lambda_\theta^2\,. \tag{18}$$

In conclusion, the strain energy can be written as a function in terms of the circumferential and axial stretch, i.e. $\widetilde{\Psi}(\lambda_\theta, \lambda_z)$. With these relations in hand, the Cauchy stress tensor $\boldsymbol{\sigma} = \partial_{\boldsymbol{F}}\Psi \cdot \mathrm{cof}\Big(\boldsymbol{F}^{-1}\Big)$ can be specified, namely

$$\boldsymbol{\sigma} = c\,\boldsymbol{F} \cdot \boldsymbol{F}^{\mathrm{t}} + 4\,k_1\,E \exp\Big(k_2\,\langle E\rangle^2\Big)\,[\,\boldsymbol{a}_1 \otimes \boldsymbol{a}_1 + \boldsymbol{a}_2 \otimes \boldsymbol{a}_2\,] \tag{19}$$

with $\boldsymbol{a}_{1,2} = \boldsymbol{F} \cdot \boldsymbol{a}_{0\,1,2}$.

Alternatively, the Cauchy stress tensor can be expressed with respect to the base system introduced in equations (2)–(4), or rather in spectral form, as

$$\sigma_{rr} = c\,\lambda_\theta^{-2}\,\lambda_z^{-2}\,, \tag{20}$$

$$\sigma_{\theta\theta} = c\,\lambda_\theta^2 + 4\cos^2\Big(\beta\Big)\,k_1\,\lambda_\theta^2\,E \exp\Big(k_2\,\langle E\rangle^2\Big)\,, \tag{21}$$

$$\sigma_{zz} = c\,\lambda_z^2 + 4\,\sin^2\Big(\beta\Big)\,k_1\,\lambda_z^2\,E \exp\Big(k_2\,\langle E\rangle^2\Big)\,. \tag{22}$$

2.2.3 Equilibrium conditions

Neglecting body forces, the underlying equilibrium conditions in terms of spatial arguments take the representation as

$$\boldsymbol{0} = \nabla_{\boldsymbol{x}} \cdot \boldsymbol{\sigma} \qquad \text{in} \qquad \mathcal{B}_t \tag{23}$$

$$\boldsymbol{t} = \boldsymbol{\sigma} \cdot \boldsymbol{n} \qquad \text{on} \qquad \partial\mathcal{B}_{to} \tag{24}$$

$$\boldsymbol{t} = -\,p_i\,\boldsymbol{n} \qquad \text{on} \qquad \partial\mathcal{B}_{ti}\,. \tag{25}$$

In view of the base system introduced in equations (2)–(4), together with the assumed coaxiality of conjugated stresses and strain measures, the Cauchy stresses allow representation in spectral form as $\boldsymbol{\sigma} = \sigma_{rr}\,\boldsymbol{e}_r \otimes \boldsymbol{e}_r + \sigma_{\theta\theta}\,\boldsymbol{e}_\theta \otimes \boldsymbol{e}_\theta + \sigma_{zz}\,\boldsymbol{e}_z \otimes \boldsymbol{e}_z$. By analogy with the derivations reviewed above and with $\boldsymbol{n} = \pm\,\boldsymbol{e}_r$, the Euler-Lagrange equations can be summarised as

$$\boldsymbol{0} = \left[\frac{\partial\sigma_{rr}}{\partial r} + \frac{\sigma_{rr} - \sigma_{\theta\theta}}{r}\right]\boldsymbol{e}_r + \frac{1}{r}\,\frac{\partial\sigma_{\theta\theta}}{\partial\theta}\,\boldsymbol{e}_\theta + \frac{\partial\sigma_{zz}}{\partial z}\,\boldsymbol{e}_z \qquad \text{in} \qquad \mathcal{B}_t$$

$$\boldsymbol{t} = \sigma_{rr}\,\boldsymbol{e}_r \qquad \text{on} \qquad \partial\mathcal{B}_{to} \tag{26}$$

$$\boldsymbol{t} = p_i\,\boldsymbol{e}_r \qquad \text{on} \qquad \partial\mathcal{B}_{ti}\,. \tag{27}$$

Due to geometrical and constitutive symmetry, the only non-trivial component of (26) is

$$\frac{\partial \sigma_{rr}}{\partial r} + \frac{\sigma_{rr} - \sigma_{\theta\theta}}{r} = 0\,, \tag{28}$$

see, for example, Ogden [22]. From this equation and the boundary condition $\sigma_{rr}|_{r=r_o} = 0$ on the outer surface of the tube, the radial Cauchy stress σ_{rr} may be calculated as

$$\sigma_{rr}(\xi) = \int_{\xi}^{r_o} [\sigma_{rr} - \sigma_{\theta\theta}] \, \frac{\mathrm{d}r}{r}\,. \tag{29}$$

The internal pressure $p_i = -\sigma_{rr}|_{r=r_i}$ is then obtained in the form

$$p_i = \int_{r_i}^{r_o} [\sigma_{\theta\theta} - \sigma_{rr}] \, \frac{\mathrm{d}r}{r}\,. \tag{30}$$

This equation plays a crucial role for the iterative numerical solution scheme of the problem considered, see Table3 for details.

2.2.4 Material parameter identification

This section deals with theoretical and algorithmic details with regard to the identification of the material parameters of the anisotropic constitutive model described in Section 2.2.2, i.e. c, k_1 and k_2. These material parameters essentially characterize the mechanical response of the artery and we therefore expect these parameters to evolve in time due to the ageing process. The objective is to determine the characteristic evolution of material parameters in time qualitatively and quantitatively on the basis of the experimental measurements.

Table 1
Setting of material, structural, geometrical and loading parameters used throughout the following computations. The fibre angle β is based on data from Ohayon et al. [23], the geometry based on data from Cilla et al. [7].

Type	Symbol	Description	Value	Unit
material	c	elastic constant	to be identified	$[kPa]$
	k_1	elastic constant	to be identified	$[kPa]$
	k_2	elastic constant	to be identified	[–]
structural	β	fibre angle	48.47	$[deg]$
geometrical	R_i	inner referential radius	0.38197	$[mm]$
	H	referential wall thickness	0.03	$[mm]$
loading	λ_z	axial stretch	1.0	[–]

In order to do so, we consider an inhomogeneous boundary value problem allowing for large deformations. Several assumptions and approximations are included into the model which shall be highlighted briefly. First, we idealize the geometrically complicated aortic specimen by the following *geometrical simplifications*; cylindrical tube, thick-walled, and singe-layered. Secondly, we idealize the experimental setting/setup by the following *boundary conditions* and *kinematic constraints*; fully incompressible, uniform internal pressure at the inner diameter of the tube, stress-free at the outer diameter of the tube, and constant axial residual stretch, circumferential residual stretch neglected. And thirdly, we idealize the material behavior by the following *constitutive assumptions*; hyperelastic, inelastic effects neglected, anisotropic (transversely isotropic or orthotropic), two mechanically equivalent families of fibres, fibres oriented in tangential plane of the tube, non-zero mechanical response of the fibres in tension-regime only, fibre dispersion neglected, and homogeneous material properties.

In order to investigate the age-dependent evolution of the material parameters in detail, we will first fit the material parameters associated with the constitutive model reviewed in Section 2.2.2 to the pressure-outer-circumferential-stretch curves recorded during the experiments. These p_i-λ_{θ_o}-curves are measured for the diseased ApoE$^{-/-}$ mice as well as for the healthy control mice, each recorded at three different locations of the aorta: the upper (thoracic) part, the lower (thoracic) part and the iliac (abdominal) part.

For the computational fitting process, we apply a *pressure-driven* parameter identification procedure, where by analogy to the experimental approach, the internal pressure p_i^{exp} is applied to the tube, see Table 2 for algorithmic details. The equilibrium condition (26) is not fulfilled a priori and therefore an additional iterative solution procedure is required. Thereby, we apply a common Newton-Raphson iteration scheme to iteratively satisfy the equilibrium condition of the underlying boundary value problem as summarized in Table 2. We are enable to compute an objective function f formulated in terms of the stretch-difference $\lambda_{\theta_o} - \lambda_{\theta_o}^{\text{exp}}$. Then, the objective function is minimized with respect to the material parameters $\boldsymbol{\nu}$, see Table 3. Generally, such minimization problems may conveniently be solved by typical optimization techniques. In this study, the Matlab optimization-algorithm `fmincon` is used which is based on a sequential quadratic programming (SQP) method. Without discussing specific algorithmic details at this stage, this algorithm allows us to find a constrained minimum of a scalar function of one or more variables, whereby initial estimate values must be set. For detailed background information on such constrained nonlinear optimization problems, the reader is referred to monographs by Luenberger [19], Bertsekas [3] and Dennis and Schnabel [10].

Finally, we end up with a set of material parameters $\boldsymbol{\nu}^{\min}$ providing optimal data fitting capabilities for the particular experimental curve of interest. The identified material parameters are then plotted over time/age in order to get an impression which parameter might be less/more affected due to the ageing effects. The corresponding results will be discussed in detail in the following Section 3.

The material parameter identification procedure is based on a sequential optimization of three material parameters c, k_1 and k_2. This procedure fits the material parameters corresponding with the first part of the test up to 3-4% of strain and c is identified with $k_1 = \text{const}$ and

Table 2
Algorithmic box for the material parameter identification procedure.

(1) set up structural and geometrical parameters from Table 1 and collect these in pseudo-vector $\boldsymbol{\kappa} = [\beta,\, R_i,\, H,\, \lambda_z]$

(2) perform initial guess $\boldsymbol{\nu} = \boldsymbol{\nu}^0 = \left[c^0,\, k_1^0,\, k_2^0\right]$ for the material parameters to be identified

(3) set objective function to $f(\boldsymbol{\nu}) = 0$

(4) identify material parameters as argument of minimum of objective function f
$\boldsymbol{\nu}^{\min} = \arg\, \min_{\boldsymbol{\nu}} f\left(\boldsymbol{\nu}; \boldsymbol{\nu}^0, \boldsymbol{\kappa}\right)$,
wherein $f(\boldsymbol{\nu})$ is determined by the algorithm for the pressure-driven case and the minimisation can be performed by, e.g., the Matlab `fmincon`-optimisation-function

Table 3
Algorithmic for the pressure-driven deformation process. All quantities are associated with t_{n+1}.

(1) given: internal pressure $p_i^{\exp}$ at time t_{n+1}

(2) perform initial guess $\lambda_{\theta_o} = \lambda_{\theta_o}^0$ for the outer circumferential stretch

(3) perform local Newton-Raphson iteration scheme

(a) compute residual
$r(\lambda_{\theta_o}) = p_i^{\exp} - p_i(\lambda_{\theta_o})$
wherein the internal pressure $p_i(\lambda_{\theta_o})$ is determined by the algorithm describen below

(b) compute linearisation of residual by means of forward difference scheme
$\mathrm{d}r = \left[r(\lambda_{\theta_o} + h) - r(\lambda_{\theta_o})\right]/h$ with $h \ll 1$

(c) Compute increment
$\Delta\lambda_{\theta_o} = \mathrm{d}r/r$

(d) compute update
$\lambda_{\theta_o} \hookleftarrow \lambda_{\theta_o} - \Delta\lambda_{\theta_o}$

(e) check tolerance with tol $\ll 1$
if $|r| <$ tol go to 4.
else go to 3. (a)

(4) compute objective function
$f(\boldsymbol{\nu}) \hookleftarrow f(\boldsymbol{\nu}) + w\left[\lambda_{\theta_o} - \lambda_{\theta_o}^{\exp}\right]^2$

$k_2 = \text{const}$ using the first two experimental data points. Later, and using the value of the elastin as seed c, we fit the rest of the parameters related with the collagen fibers, so k_1 and k_2 are identified with $c = \text{const}$ using all experimental data points [27]. This non-standard sequential optimization technique is applied, as it may occur that a single optimization including every experimental data point for all of the three material parameters results in unphysical material parameters, e.g. such that $c < 0$, or in $c = \texttt{lb}$ for a constrained optimization including a lower bound `lb`.

Table 4
Algorithmic for the determination of the internal pressure.

(1) given: material parameters $\boldsymbol{\nu} = [c,\ k_1,\ k_2]$, structural and geometrical parameters $\boldsymbol{\kappa} = [\beta,\ R_i,\ H,\ \lambda_z]$, see Table 1, deformation in terms of the outer circumferential stretch λ_{θ_o} at time t_{n+1}

(2) calculate referential outer radius
$R_o = R_i + H$

(3) calculate current radii
$r_o = \lambda_{\theta_o} R_o$
$r_i = \sqrt{r_o^2 - \left[R_o^2 - R_i^2\right]/\lambda_z}$

(4) apply $m = 3$-point Gaussian quadrature rule with quadrature points $\xi_j = \left\{ -\sqrt{3/5} \ \ 0 \ \ \sqrt{3/5} \right\}$ and weights $w_j = \left\{5/9 \ \ 8/9 \ \ 5/9\right\}$:
loop over number of quadrature points $j = 1, \ldots, m$

(a) calculate current radius
$r_j = [[r_i + r_o] + \xi_j\,[r_o - r_i]]/2$

(b) calculate referential radius
$R_j = \sqrt{\lambda_z\left[r_j^2 - r_i^2\right] + R_i^2}$

(c) calculate circumferential stretch
$\lambda_{\theta j} = r_j / R_j$

(d) calculate radial and circumferential stresses
$\sigma_{rrj} = c\,\lambda_{\theta j}^{-2}\,\lambda_z^{-2}$
$\sigma_{\theta\theta j} = c\,\lambda_{\theta j}^2 + 4\cos^2\left(\beta\right) k_1\,\lambda_{\theta j}^2\,E \exp\left(k_2\,\langle E\rangle^2\right)$
with $E = \lambda_z^2 \sin(\beta)^2 + \lambda_{\theta j}^2 \cos(\beta)^2 - 1$ by means of equations (20, 21)

calculate internal pressure
$p_i \approx [r_o - r_i]/2 \sum_{j=1}^{m} \left[\sigma_{\theta\theta j} - \sigma_{rrj}\right]\ w_j / r_j$

3 Results

This section summarizes the results obtained by the associated simulation framework to the experiments discussed in the previous section.

3.1 Mechanical properties

In order to illustrate the stiffening behaviour with respect to age, we plot the experimentally obtained circumferential stretch over different stages of ageing at three chosen pressure levels, i.e. $p_i = \{50,\ 150,\ 250\}[weeks]$ in Figure 2. The left column (a,c,e) corresponds to the diseased ApoE$^{-/-}$ mice, the right column (b,d,f) corresponds to the healthy control mice. The three different rows (a,b), (c,d), (e,f) are associated with different locations over the length of the

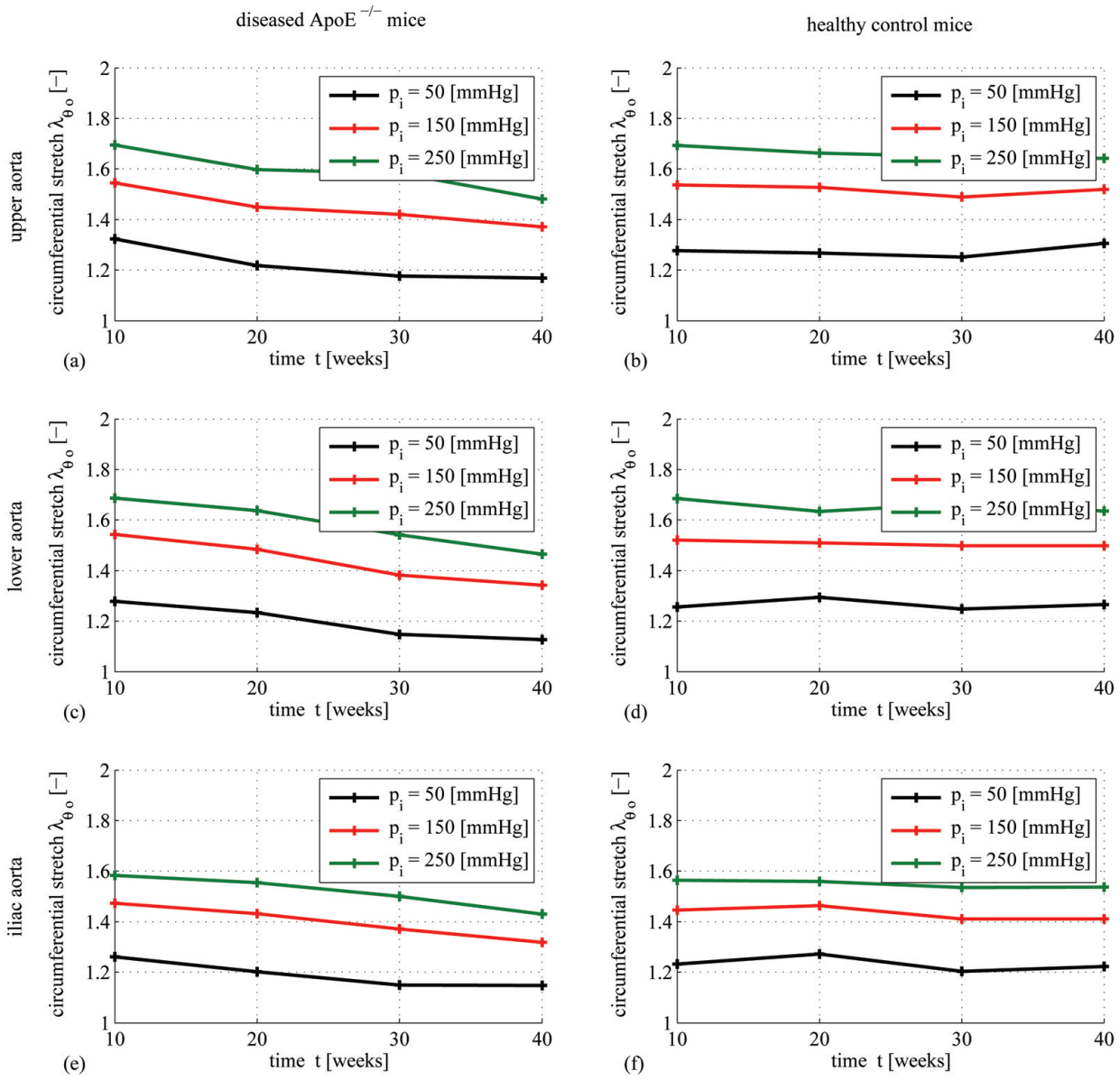

Fig. 2. Experimentally obtained circumferential stretch with respect to different stages of ageing at three chosen pressure levels, i.e. $p_i = \{50, 150, 250\}[weeks]$. The left column (a,c,e) corresponds to the diseased ApoE$^{-/-}$ mice, the right column (b,d,f) corresponds to the healthy control mice. The three different rows (a,b), (c,d), (e,f) are associated with different locations over the length of the considered arterial specimen [7].

considered arterial specimen. We observe that the circumferential stretch λ_{θ_o} decreases with age (stiffening) for the diseased ApoE$^{-/-}$ mice but stays relatively constant for the healthy control mice.

As it was pointed in Cilla et al. [7], the ApoE$^{-/-}$ aorta stiffness increases dramatically for increasing diet period. This holds for all aortic zones studied. In contrast, the aorta stiffness of the control mice remains practically constant for increasing diet period. Comparing the

ApoE$^{-/-}$ and control results, the ApoE$^{-/-}$ pressure-stretch curve after 10 [*weeks*] for the upper aorta and 10 and 20 [*weeks*] for the lower and iliac aorta, are similar to the control curves for all ages. This shows that a short period on a hyper-lipidic diet does not significantly affect the mechanical properties of the ApoE$^{-/-}$ mice. Furthermore, the different behaviour of the three zones studied for the ApoE$^{-/-}$ mice is highlighted. The upper aorta turns out to be stiffer than the lower aorta which, in turn, is stiffer than the iliac aorta. The stiffness for the three zones considered for the control mice remains constant.

3.2 Material parameter identification

This section summarizes the results of the material parameter identification of the anisotropic constitutive model described in Section 2.2.2, i.e. c, k_1 and k_2. These material parameters, which characterize the mechanical response of the artery, are expect to evolve in time due to the ageing process. In this regard, the objective is to determine the characteristic evolution of material parameters in time qualitatively and quantitatively on the basis of the experimental measurements.

The internal pressure p_i^{exp}, i.e. the quantity which is actually *prescribed* in the experiments, is applied to the tube, see Table 4 for algorithmic details.

The fitting results of the material parameter identification procedure are depicted in Figure 3 where the discrete points represent the original experimental data from [7], and the solid lines represent the associated (simulated) fitting. The identified material parameters are summarized in Table 5 and their temporal evolution is illustrated in Figure 4. The results in Figure 3 show excellent fitting capabilities.

With regard to the temporal evolution of the material parameters depicted in Figure 4, we, on the one hand, expect the material parameters for the control mice aortas for one single location to remain almost constant. However, it becomes apparent, that the parameters quite strongly deviate from each other with respect to time, see, for instance, parameter k_2 in Figure 4(d). On the other hand, we expect the material parameters for the ApoE$^{-/-}$ mice aortas for one single location to exhibit a characteristic increase or decrease in time. And indeed, we observe that, e.g. parameter c first increases linearly within $t = 10 - 30\,[weeks]$ and saturates for $t = 30 - 40\,[weeks]$, see Figure 4(a). A similar behaviour holds for parameter k_1, Figure 4(b), whereas k_2, Figure 4(c), remains almost constant within $t = 10 - 30\,[weeks]$ and then increases for $t = 30 - 40\,[weeks]$.

4 Discussion

The objective of this work consists in the qualitative and quantitative analysis of ageing processes and associated plaque formation in mice arteries which are typical for atherosclerosis.

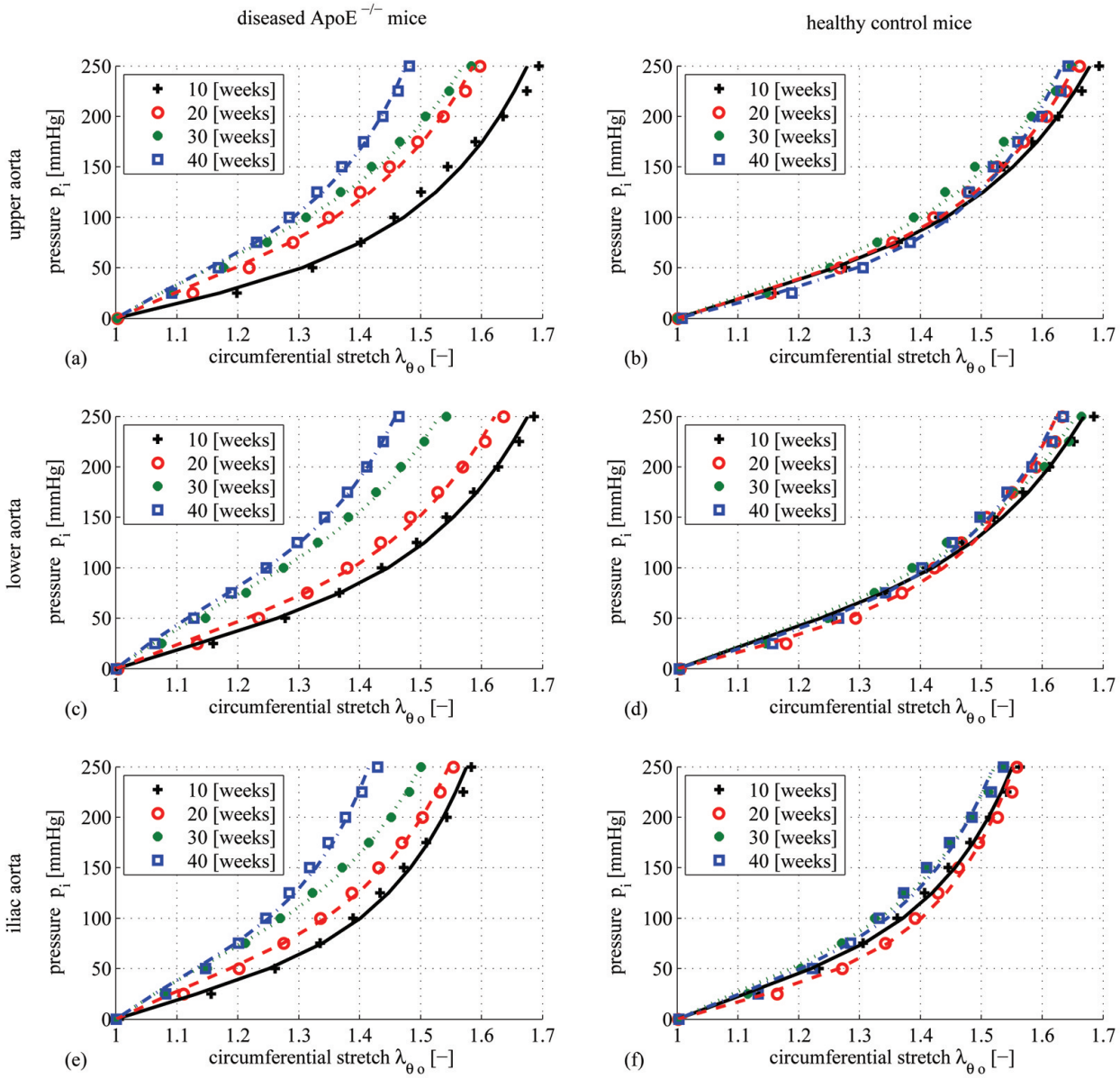

Fig. 3. Fitted experimental data based on the material parameter identification procedure. The discrete points represent the original experimental data from [7], the lines the associated (simulated) fitting. The material parameter identification procedure is based on a sequential optimization of three material parameters c, k_1 and k_2: in a first step parameter c is identified with $k_1 = \text{const}$ and $k_2 = \text{const}$ using the first two experimental data points, in a second step k_1 and k_2 are identified with $c = \text{const}$ using all experimental data points.

Specifically, reliable information on the characteristic evolution of *pressure-stretch curves* and *axial residual stretches* due to the ageing effects are extracted from appropriate experiments. Furthermore, characteristic *age-dependent material parameters* are identified on the basis of a continuum-mechanics-based parameter optimization technique. Complex experimental investigations are performed on the one hand, while, on the other, a continuum-mechanics-based material modelling approach is used to identify characteristic age-dependent sets of mate-

Table 5
Identified material parameters by means of the pressure-driven material parameter identification procedure.

		diseased ApoE$^{-/-}$ mice				healthy control mice			
	$[weeks]$	10	20	30	40	10	20	30	40
upper aorta	$c\,[kPa]$	13.92	54.83	85.38	89.74	32.09	35.80	39.87	18.29
	$k_1\,[kPa]$	116.70	155.08	167.36	160.41	128.96	125.49	142.81	113.99
	$k_2\,[-]$	1.20	1.33	1.21	2.69	1.00	1.19	1.14	1.57
lower aorta	$c\,[kPa]$	32.51	49.31	116.15	142.56	40.50	22.36	40.69	33.81
	$k_1\,[kPa]$	123.90	142.81	171.43	158.89	136.79	118.49	150.56	131.24
	$k_2\,[-]$	1.06	1.19	1.42	2.71	0.95	1.57	0.90	1.37
iliac aorta	$c\,[kPa]$	34.38	67.61	108.09	105.12	48.10	29.62	62.78	49.29
	$k_1\,[kPa]$	122.75	144.24	173.31	180.15	132.20	112.06	150.12	147.65
	$k_2\,[-]$	1.99	1.89	1.89	3.81	2.11	2.52	2.18	2.33

rial parameters. A computational continuum-mechanics-based framework is used to identify age-dependent material parameters on the basis of the experimental data. We consider an inhomogeneous boundary value problem allowing for large deformations, i.e. an incompressible thick-walled cylindrical tube, which is assumed to approximate a real artery. The basic deformation modes considered are represented by combined inflation and axial extension. We make use of an orthotropic constitutive model with two families of fibres and solve the underlying equilibrium conditions iteratively. We compute an objective function, represented by the difference between simulated and experimental data, which is minimized with respect to the material parameters. As a main objective, we aim at determining the characteristic age-dependent evolution of material parameters in time.

Generally, the results show excellent fitting capabilities. Similar results were obtained by [6], they applied a fiber-based constitutive model to mechanical data from aorta during postnatal development of WT and Eln+/- mice and obtained the model was capable of distinguishing elastin amounts and identifying trends during development. Regarding the temporal evolution of the material parameters, we observe significant deviations of the material parameters between the ApoE$^{-/-}$ and the control mice as well as for the different locations over the aorta (upper, lower, iliac) which clearly underlined our observations from the experiments. With regard to the temporal evolution of the material parameters, we, on the one hand, expect the material parameters for the control mice aortas for one single location to remain almost constant. However, it became apparent, that the parameters quite strongly deviate from each other with respect to time. On the other hand, we expected the material parameters for the ApoE$^{-/-}$ mice aortas for one single location to exhibit a characteristic increase/decrease in time. We indeed observed that, parameter c first increases linearly within $t = 10 - 30\,[weeks]$

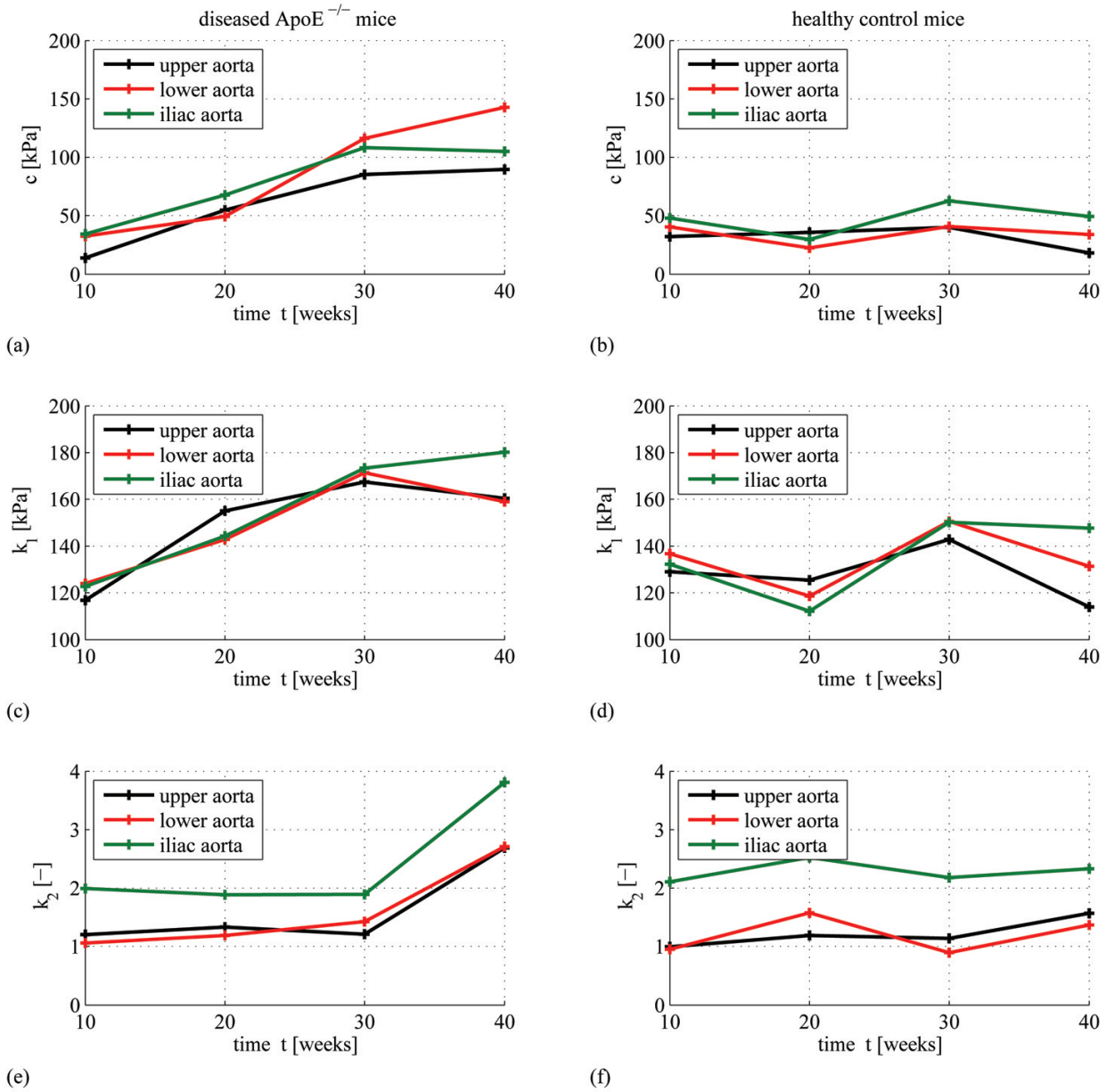

Fig. 4. Material parameter evolution for the stress-driven (pressure-driven) parameter identification procedure plotted over time, associated values given in Table 5. The left column (a,c,e) corresponds to the diseased ApoE$^{-/-}$ mice, the right column (b,d,f) corresponds to the healthy control mice.

and saturates for $t = 30 - 40\,[weeks]$. A similar behavior could be identified for parameter k_1 whereas k_2 remained almost constant within $t = 10 - 30\,[weeks]$ and then increased for $t = 30 - 40\,[weeks]$. No study with all these characteristics can be found in the literature. Only Agianniotis and Stergiopulos [**?**] compared the mechanical properties of young 10-12 week-old ApoE$^{-/-}$ mice without fat diet with C57BL/6J wild-type mice by extension-inflation mechanical tests. However, they only compute the Hudetz incremental elastic modulus.

It should be pointed out that the study presented here has some limitations and that the results

could be improved in future works. First, the application of an inhomogeneous incompressible thick-walled cylindrical tube which should represent a real artery is a significant idealization and simplification. For future studies, a non-cylindrical multi-layered problem setting should be considered at least. Furthermore, circumferential residual stretches should be taken into account as well as the effects of fibre dispersion. However, this essentially requires the acquisition of related experimental data which, in turn, is a non-trivial task, and therefore, was not available at this stage. In addition, since these inflated tests are performed *in situ*, the measurement of longitudinal forces, and thus the longitudinal stiffness can not be assessed. *Ex situ* inflation test combined with extension test could be carried out. However the control of the liquid leaks in this kind of test is difficult to achieve due to the great number of branches of the aortic root. The second consideration concerns the size of the mouse aorta. Although the mice were dissected carefully, there are many branches in the aortic root which usually lead to small leaks during the inflation test.. Another crucial aspect associated with experiment and simulation consists in the appropriate incorporation of axial residual stretches during the measurements and their associated consideration within the parameter identification process. As pointed out above, we observe that the outer circumferential stretch λ_{θ_o} is one for zero pressure for all experimental pressure-outer-circumferential-stretch-curves. From the physical point of view, this remains questionable, as we would rather expect the outer circumferential stretch to be smaller than one, due to the influence of the present axial residual stretch. However, at this stage, no reliable data for the proper incorporation of axial residual stretches is available and therefore this approach constitutes future research.

In spite of these limitations, the obtained results are promising and demonstrate substantial changes in the mechanical behaviour and in the structural properties of ApoE$^{-/-}$ mice aortas as compared to the control group. These findings are important for a better understanding of the cardiovascular system of mice and could serve as a reference for future investigations of mechanical properties of blood vessels suffering atherosclerotic diseases.

5 Acknowledgments

Support from the Spanish Ministry of Economy and Competitiveness through the research projects DPI2010-20746-C03-01 and PRI-AIBDE-2011-1216, the CIBER initiative and the Platform for Biological Tissue Characterization of CIBER-BBN, and from the University of Zaragoza through the research project UZ2008-BIO-21 is highly appreciated. Include acknowledgments Dormunt

References

[1] Alastrué, V., Martínez, M., Doblaré, M., Menzel, A., 2009. Anisotropic micro-sphere-based finite elasticity applied to blood vessel modelling. Journal of the Mechanics and Physics of Solids 57, 178–203.

[2] Arroyo, L. H., Lee, R. T., 1998. The unstable atheromatous plaque. Canadian Journal of Cardiology 14, 11B–13B.

[3] Bertsekas, D. P., 1996. Constrained Optimization and Lagrange Multiplier Methods. Vol. 4 of Athena Scientific Optimization and Computation Series. Athena Scientific.

[4] Boehler, J. (Ed.), 1987. Applications of Tensor Functions in Solid Mechanics. No. 292 in CISM Courses and Lectures. Springer.

[5] Buja, L., Kita, T., Goldstein, J., Watanabe, Y., Brown, M., 1983. Cellular pathology of progressive atherosclerosis in the WHHL rabbit. An animal model of familial hypercholesterolemia. Arteriosclerosis, Thrombosis, and Vascular Biology 3 (1), 87–101.

[6] Cheng, J. K., Stoilov, I., Mecham, R. P., Wagenseil, J. E., 2013. A fiber-based constitutive model predicts changes in amount and organization of matrix proteins with development and disease in the mouse aorta. Biomech Model Mechanobiol 12, 497–510.

[7] Cilla, M., Pérez, M. M., Peña, E., Martínez, M. A., 2014. Arterial Stiffening due to atherosclerosis in ApoE$^{-/-}$ mice. Effect of diet and age submitted for publication.

[8] Daugherty, A., 2002. Mouse models of atherosclerosis. American Journal of the Medical Sciences 323 (1), 3–10.

[9] Davis, E. C., 1995. Elastic lamina growth in the developing mouse aorta. Journal of Histochemistry & Cytochemistry 43 (11), 1115–23.

[10] Dennis, Jr.,, J., Schnabel, R., 1996. Numerical Methods for Unconstrained Optimization and Nonlinear Equations. No. 16 in Classics in Applied Mathematics. SIAM.

[11] Faggiotto, A., Ross, R., Harker, L., 1984. Studies of hypercholesterolemia in the nonhuman primate. I. Changes that lead to fatty streak formation. Arteriosclerosis, Thrombosis, and Vascular Biology 4 (4), 323–340.

[12] García, A., Peña, E., Laborda, A., Lostalé, F., Gregorio, M. A. D., Doblaré, M., Martínez, M. A., 2011. Experimental study and constitutive modelling of the passive mechanical properties of the porcine carotid artery and its relation to histological analysis. Implications in animal cardiovascular device trials. Medical Engineering & Physics 33, 665–676.

[13] Gasser, T., Ogden, R., Holzapfel, G., 2006. Hyperelastic modelling of arterial layers with distributed collagen fibre orientations. Journal of the Royal Society Interface 3, 15–35.

[14] Guo, X., Kassab, G. S., 2003. Variation of mechanical properties along the length of the aorta in C57BL/6 mice. American Journal of Physiology - Heart and Circulatory Physiology 285, H2614–H2622.

[15] Holzapfel, G., Gasser, T., Ogden, R., 2000. A new constitutive framework for arterial wall mechanics and a comparative study of material models. Journal of Elasticity 61, 1–48. URL `http://dx.doi.org/10.1023/A:1010835316564`

[16] Huang, Y., Guo, X., Kassab, G. S., 2006. Axial nonuniformity of geometric and mechanical properties of mouse aorta is increased during postnatal growth. American Journal of Physiology - Heart and Circulatory Physiology 290 (2), H657–H664.

[17] Jawien, J., Nastalek, P., Korbut., R., 2004. Mouse models of experimental atherosclerosis. Journal of Physiology and Pharmacology 55 (3), 503–517.

[18] Lee, R. T., Libby, P., 1997. The unstable atheroma. Arteriosclerosis, Thrombosis, and Vascular Biology 17, 1859–1867.

[19] Luenberger, D., 1984. Nonlinear Programming, 2nd Edition. Addison–Wesley.

[20] Machii, M., Becker, A. E., 1997. Morphologic features of the normal aortic arch in neonates, infants, and children pertinent to growth. The Annals of Thoracic Surgery

64 (2), 511–515.
[21] Nakashima, Y., Plump, A., Raines, E., Breslow, J., Ross, R., 1994. ApoE-deficient mice develop lesions of all phases of atherosclerosis throughout the arterial tree. Arteriosclerosis, Thrombosis, and Vascular Biology 14 (1), 133–140.
[22] Ogden, R., 1997. Non–Linear Elastic Deformations. Dover.
[23] Ohayon, J., Mesnier, N., Broisat, A., Toczek, J., Riou, L., Tracqui, P., 2012. Elucidating atherosclerotic vulnerable plaque rupture by modeling cross substitution of ApoE$^{-/-}$ mouse and human plaque components stiffnesses. Biomechanics and Modeling in Mechanobiology 11 (6), 801–813.
URL http://dx.doi.org/10.1007/s10237-011-0353-8
[24] Plump, A., Smith, J., Hayek, T., Aalto-Setala, K., Walsh, A., Verstuyft, J., Rubin, E., Breslow., J., 1992. Severe hypercholesterolemia and atherosclerosis in apolipoprotein E-deficient mice created by homologous recombination in ES cells. Cell 71 (2), 343–353.
[25] Reitman, J., Mahley, R., Fry, D., 1982. Yucatan miniature swine as a model for diet-induced atherosclerosis. Atherosclerosis 43 (1), 119–132.
[26] Schwartz, C. J., Sprague, E. A., Kelley, J. L., Valente, A. J., Suenram, C. A., 1985. Aortic intimal monocyte recruitment in the normo and hypercholesterolemic baboon (*Papio Cynocephalus*). Virchows Archiv 405, 175–191.
[27] Sáez, P., Peña, E., Martínez, M. A., 2014. A structural approach including the behavior of collagen cross-links to model patient-specific human carotid arteries. Ann Biomed Eng 42, 1158–1169.
[28] Spencer, A., 1972. Deformations of Fibre-Reinforced Materials. Oxford University Press.
[29] Spencer, A. (Ed.), 1984. Continuum Theory of the Mechanics of Fibre-Reinforced Composites. No. 282 in CISM Courses and Lectures. Springer.
[30] Tracqui, P., Broisat, A., Toczek, J., Mesnier, N., Ohayon, J., Riou, L., 2011. Mapping elasticity moduli of atherosclerotic plaque in situ via atomic force microscopy. Journal of Structural Biology 174, 115–123.
[31] Wagner, W. D., 1978. Risk factors in pigeons genetically selected for increased atherosclerosis susceptibility. Atherosclerosis 31 (4), 453–463.
[32] Wells, S. M., Langille, B. L., Lee, J. M., Adamson, S. L., 1999. Determinants of mechanical properties in the developing ovine thoracic aorta. American Journal of Physiology - Heart and Circulatory Physiology 277 (4), H1385–H1391.
[33] Wong, L. C. Y., Langille, B. L., 1996. Developmental Remodeling of the Internal Elastic Lamina of Rabbit Arteries: Effect of Blood Flow. Circulation Research 78 (5), 799–805.
[34] Zhang SH, Reddick RL, P. J., N., M., Oct 1992. Spontaneous hypercholesterolemia and arterial lesions in mice lacking apolipoprotein E. Proceedings of the National Academy of Sciences of the United States of America 258 (5081), 468–471.